The Realization of Praseodymium Nickelate Based IT-SOFC Cathode by Physical Deposition: Reactive Magnetron Sputtering Combined with Annealing Treatment

Xiaolei YE[1, 2], Hang LUO[1, 2], Lei GAO[1, 2*], Li Yang[1, 2*], Shenghui GUO [1, 2*], Ming HOU [1, 2], Kaihua CHEN[1, 2],Yunchuan LI [1, 2], Zhiguang HUA[3], Pascal BRIOIS[4]

1. Faculty of Metallurgical and Energy Engineering, Kunming University of Science and Technology, Kunming 650093, China

2. State Key Laboratory of Complex Nonferrous Metal Resources Clean Utilization; Faculty of Metallurgical and Energy Engineering, Kunming University of Science and Technology, Kunming 650093, China

3. School of Automation, Northwestern Polytechnical University, Xi'an, 710129, China

4. FEMTO-ST Institute (UMR CNRS 6174), UBFC/UTBM. Site de Montbéliard, F-90010 Belfort-France

Corresponding authors: Lei GAO (glkust2013@hotmail.com); Li YANG (yanglikmust@163.com); Shenghui GUO (shguo78@hotmail.com)

Abstract: The simplified preparation of high-performance cathode layers is crucial for advancing the widespread commercial utilization of solid oxide fuel cells (SOFCs). This investigation centers on achieving $Pr_2NiO_4@Pr_6O_{11}$ (PPNO) through reactive magnetron sputtering (RMS) under the monitoring of a plasma emission monitoring system (PEM) in conjunction with annealing treatment. By utilizing the PEM system, a Setpoint of 70 % was selected to enable a rapid deposition rate of Pr-O oxide. Subsequently, a Pr-Ni-O oxide with an appropriate Pr/Ni atomic ratio was deposited by regulating the power applied to the Ni target. The PPNO cathode layer was formed through the annealing of Pr-Ni-O oxide (at 1000 °C for 30 min). Moreover, the porosity evolution of the PPNO cathode layer was elucidated. The deposited PPNO cathode demonstrates a remarkably low polarization resistance (R_p) of 0.08 $\Omega \cdot cm^2$ at 750 °C. The assembled NiO-YSZ|YSZ|GDC|PPNO single cell achieves a notable power density of 1155 $mW \cdot cm^{-2}$ at 750 °C. Furthermore, the single cell experiences only 6.9 % decay after 65 h of stability testing at 700 °C, indicating interesting long-term stability. This research introduces a fresh perspective on the realizing high-performance IT-SOFC cathode layers.

Keywords: IT-SOFC, Reactive magnetron sputtering, PPNO, Porous cathode layer

1. Introduction

The SOFCs were hailed as a promising technology for energy conservation and carbon emission reduction. Current SOFCs operate at high temperatures (800 -1000 °C) to enhance electrochemical kinetics, eliminating the need for costly precious metal catalysts [1-3]. Despite the benefits of high-temperature SOFCs (HT-SOFCs), challenges such as expensive interconnects and sealants, as well as accelerated material degradation at high temperatures, impede their widespread implementation in energy systems. Intermediate-temperature SOFC (IT-SOFC), operating between 600 - 800 °C, address the drawbacks of HT-SOFCs while providing notable economic advantages [4]. However, reducing the operating temperature diminishes the oxygen reduction reaction (ORR) activity at the cathode, as ORR is a thermally activated process [5]. Therefore, enhancing cathode electrochemical activity to decrease cathode polarization resistance is crucial for advancing IT-SOFC technology.

Materials exhibiting mixed ionic and electronic conductivity (MIEC) are highly regarded for addressing the issue of increased cathode polarization resistance at lower operating temperatures [6, 7]. In MIEC cathodes, three-phase boundaries (TPBs) can

be expanded across the entire electrolyte surface, as opposed to being confined to the electrolyte/electrode interface, thereby effectively mitigating cathode polarization resistance. Recently, K_2NiF_4-type $Ln_2NiO_{4+\delta}$ compounds (Ln = La, Pr, Nd) have emerged as promising candidates due to their exceptional oxygen reduction catalytic activity, robust MIEC behavior across a wide range of oxygen partial pressures, and favorable chemical compatibility with common electrolytes and metal interconnects. [8, 9]. Consequently, $Ln_2NiO_{4+\delta}$ compounds are being considered as prospective cathode materials for IT-SOFC [8]. In the realm of IT-SOFCs, while wet deposition is a well-established technique for depositing thick cathode layers, the use of thicker cathode layers may not be cost-effective in terms of raw material consumption [10]. The use of RMS enables the deposition of thin and dense layers in IT-SOFCs components, leading to reduced ohmic losses. This method is highly favored for fabricating electrolytes [11] or barrier layers [12] in IT-SOFCs. Encouraging outcomes have been reported in the fabrication of half-cells employing RMS technology [13]. Our previous investigations have illustrated the feasibility of utilizing RMS technology for depositing cathode layers by co-sputtering various metal targets [14]. However, electrochemical assessments and single-cell evaluations of the deposited $La_2NiO_{4+\delta}$ cathode exhibited subpar performance. The power density of the Ni-YSZ|YSZ|GDC| $La_2NiO_{4+\delta}$ single cell reached only 71 mW·cm^{-2} at 700 °C [14]. This underperformance is related to the impermeability of the dense $La_2NiO_{4+\delta}$ cathode layer, which impedes the rapid adsorption and diffusion of oxygen, resulting in inferior reactivity compared to other MIECs [13, 15]. Therefore, to fully exploit the exceptional electrochemical properties of a thin cathode layer deposited using RMS technology, enhancing its porosity is crucial.

This study, examines the rapid deposition of a porous PPNO composite under unstable plasma conditions using PEM [16], with a systematic investigation into pore formation and morphological evolution of the PPNO composite. Subsequently, a NiO-YSZ|YSZ|GDC|PPNO single cell was produced on a commercial NiO-YSZ anode employing RMS technology. The single cell exhibited exceptional electrochemical performance attributed to the synergistic effect of the PPNO cathode's superior catalytic activity and optimized porous structure.

2. Experimental procedure

2.1 Magnetron sputtering equipment

Samples were deposited in a sputtering chamber (Alcatel SCM650) with a PEM system. The sputtering chamber is cylindrical, measuring 300 mm in height and 620 mm in internal diameter. The RMS device utilizes a dual-channel DC Pinnacle® Plus+ generator, allowing pulse frequencies adjustable from 5 to 350 kHz. The substrate holder, 610 mm in diameter, was positioned 70 mm from the target and rotated at 14 revolutions per minute (RPM) via a motor drive system. The chamber's vacuum level was monitored by a pressure gauge, which showed a limit of 10^{-3} mbar. The PEM system comprises a fiber optic probe, a conductive fiber, a spectrometer, and a photomultiplier tube, all managed via a computer interface for real-time monitoring of the plasma emission spectrum. The fiber optic probe was positioned near the Pr target to capture the emission signal, specifically focusing on the 422 nm spectral line of Pr. Custom LabVIEW® software analyzes and adjusts the spectral signal intensity, enabling precise deposition control.

2.2 Experimental materials and cell realization

The target materials Pr and Ni (99.9%, Φ 200 × 6 mm) were sourced from AMPERE INDUSTRIE, while 8YSZ and NiO-YSZ (Φ 25 × 0.5 mm) were obtained from NEYCO. Symmetric PPNO/8YSZ/PPNO cells were created by depositing PPNO cathode layers on dense 8YSZ pellet. The YSZ|GDC electrolyte layer was deposited on NiO-YSZ to form a half-cell (NiO-YSZ|YSZ|GDC) [17]. Subsequently, a PPNO cathode was deposited on the NiO-YSZ|YSZ|GDC via magnetron sputtering to fabricate a NiO-YSZ|YSZ|GDC|PPNO single cell. Annealing of the symmetric and single cells occurs in air using a standard furnace (Borel, Switzerland). The symmetrical and single cells were then shaped into round (Φ 11mm) and square (11 × 11 mm) button cells, respectively, to accommodate electrochemical measurement equipment.

2.3 Characterization and cells testing

Structural characterization was performed with a BRUKER D8 XRD using Co Kα radiation. Surface and cross-sectional morphologies were studied using a JEOL JSM-7800F scanning electron microscope (SEM) with nanoscale resolution. Cross-sectional SEM images enabled porosity analysis of PPNO using ImageJ 2.0. Electrochemical impedance spectroscopy (EIS) was performed using Garmy 1000E electrochemical workstation coupled with a high-temperature furnace (OTF-1200X).

Impedance spectra were recorded from 600 °C to 750 °C at 50 °C intervals with a sinusoidal voltage perturbation of 10 mV. The frequency range during EIS testing was from 10^{-1} to 10^6 Hz. The current–voltage-power (I–V–P) discharge characteristics of the cell were measured using a CS1350 electrochemical workstation. Prior to testing, hydrogen was introduced into the anode at 60 mL/min for 3 h to reduce NiO at 750 °C. During the test, hydrogen was humidified by passing it through water before entering the anode, while oxygen was supplied to the cathode at 40 mL/min.

3. Result and discussion

3.1 Deposition for Pr-Ni-O coatings

The rapid deposition of Pr-Ni-O oxides is essential for preparing PPNO composite cathodes. The deposition process of the Pr-Ni-O coatings, using Pr and Ni targets, was monitored via the optical emission intensity of the Pr target at 422 nm near the target area. The collected information was transmitted to a computer to regulate the oxygen flow rate, maintaining the emission intensity between approximately 25% (fully oxidized target) and 100% (in pure argon), as depicted **Fig. 1**. Initially in a pure argon atmosphere, the deposition mode transitioned from metallic to oxide as the O_2 flow rate increased to 7 sccm. Conversely, reducing the O_2 flow to 3.2 sccm switched the deposition back to the metallic mode. The deposition region with an O_2 flow rate of 3.2 to 7 sccm was identified as an unstable deposition region for Pr-Ni-O coating. The Ni target voltage was monitored in real time against the O_2 flow rate at a constant power of 111 W. The resulting hysteresis loop of the Ni target voltage exhibited a similar trend to the relationship between the optical emission intensity of the Pr target and the O_2 flow rate. Notably, the unstable deposition regions for both targets largely coincided, as shown by the hysteresis loops in **Fig.1**.
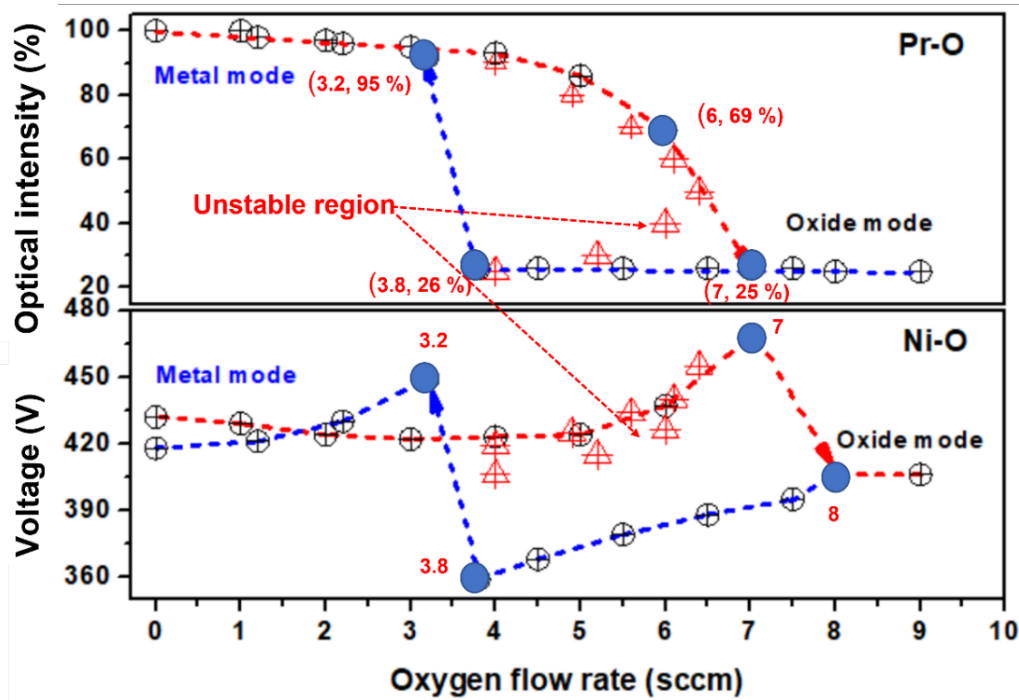
Fig.1 The evolution of the emission optical intensity of the Pr (422nm) target and the voltage of Ni target with the introduction of oxygen flow

To determine the optimal emission optical intensity (Setpoint) for Pr target in depositing Pr-Ni-O coatings, both deposition rate and coating structure were examined across various Setpoints. **Tab.1** outlines key deposition parameters. The optical emission Setpoints for Pr target were adjusted to 50 %, 60 %, and 70 % with the Ni target power held constant at 111 W. **Fig.2a**, demonstrates a linear increase in deposition rate with higher Setpoints on the Pr target. Furthermore, **Fig.2 b** indicates that the Pr:Ni atomic ratio rises with increased Setpoints, attributed to the enhanced power applied to the Pr target, as detailed in **Tab.1**. XRD patterns in **Fig.3**, reveal that coatings deposited at 50 % and 60 % Setpoints on the Pr target primarily consist of nanocrystalline or poorly crystalline PrOx. In contrast, the coating at a 70 % Setpoint predominantly features cubic Pr_6O_{11}, along with minor amounts of NiO and metallic Pr. Despite the presence of some metallic Pr at 70%, this Setpoint offers significant advantages in deposition rate and Pr-Ni-O coating crystallinity compared to 50 % and 60 %.

Table 1 The RMS deposition parameters of Pr-Ni-O coatings

Parameters	Pr target	Ni target
Ar flow rate (sccm)	200	
O_2 flow rate (sccm)	3.8-7.0	
Total pressure (Pa)	1.97-2.02	
D_{s-t} (mm)	70	
Frequency (kHz)	50	
T_{off} (μs)	4	
Voltage (V)	203-235	390-479
Current (A)	2.5	0.23-0.35
Power (W)	510-630	111-160
Setpoint (%)	50-70	–

D_{s-t}: Distance between substrate and target
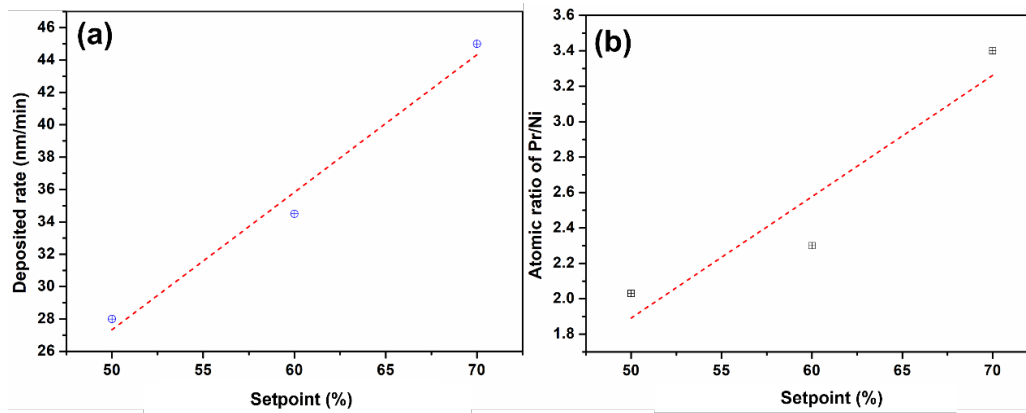
Fig.2 (a) Deposition rate and (b) atomic ratio of Pr/Ni as a function of optical emission Setpoint on Pr target
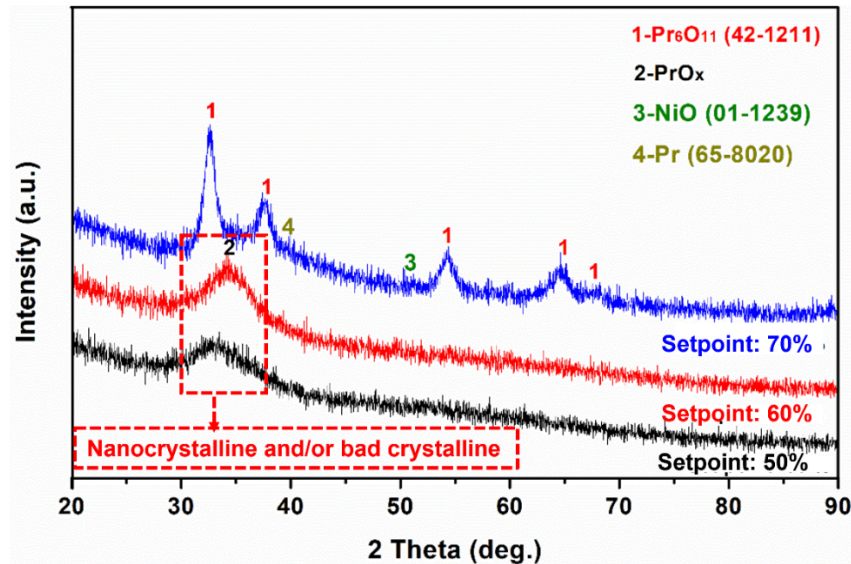
Fig.3 XRD patterns of Pr-Ni-O coatings deposited on glass slides with different optical emission Setpoints on Pr target

Pr-Ni-O coatings were deposited with varying Pr/Ni atomic ratios by adjusting the Ni target power, maintaining an optical emission setpoint of 70 % on Pr target. Energy-dispersive spectroscopy (EDS) determined the Pr/Ni atomic ratio, revealing a linear

decrease in this ratio with increased Ni target power, while the deposition rate increased linearly (**Fig.4**). The phase composition of the Pr-Ni-O coatings was analyzed by XRD post-annealing at 1000 °C for 30 min. As illustrated in **Fig. 4** coatings with high Pr/Ni ratios (6.1 and 3.4) mainly consisted of Pr_2NiO_4 and Pr_6O_{11} phases. Conversely, coatings with a Pr/Ni ratio of 1.4 largely comprised Pr_6O_{11} and minor nickel oxides (NiO and Ni_2O_3). At a Pr/Ni ratio of 2.0, both Pr_6O_{11} and $Pr_4Ni_3O_{9.85}$ were present, indicating partial decomposition of Pr_2NiO_4. A Pr/Ni ratio of 1.6 predominantly featured Pr_2NiO_4, with traces of NiO, likely due to Pr deficiency.

These results suggest that a higher Pr/Ni atomic ratio is necessary to achieve a composite PPNO coating comprising both Pr_2NiO_4 and Pr_6O_{11}. Comparison of XRD patterns for coatings with Pr/Ni ratios of 3.4 and 6.1 indicates that the relative content of Pr_2NiO_4 and Pr_6O_{11} can be adjusted by modifying the Pr/Ni ratio. Consequently, an optical emission setpoint of 70 % on the Pr target is optimal for depositing high-quality PPNO cathodes.
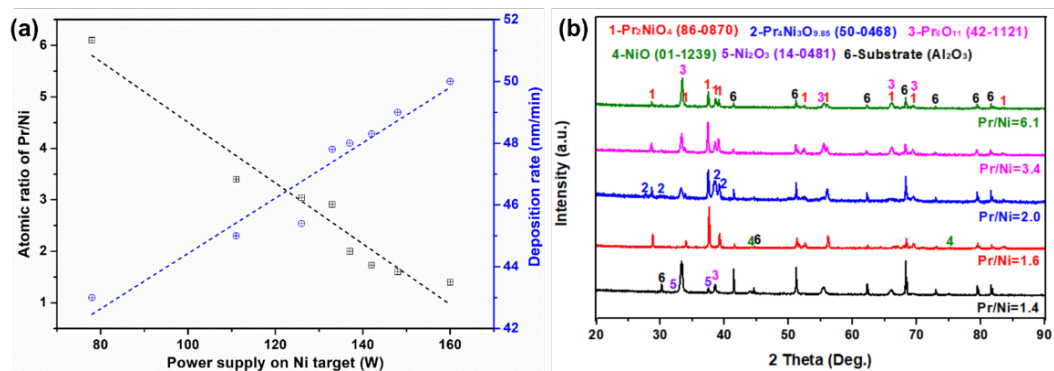

Fig. 4 (a) Deposition rate and Pr/Ni atomic ratio of the Pr-Ni-O coating deposited with different powers on the Ni target; (b) XRD of Pr-Ni-O coatings with different atomic ratios post-annealing at 1000 °C for 30 min

3.2 The realization of PPNO cathode

PPNO cathodes were achieved by depositing Pr-Ni-O coatings with a high Pr/Ni atomic ratio, specifically at a 70 % setpoint on the Pr target. Deposition parameters were detailed in **Tab. 2**. The structural and morphological evolution of PPNO cathode coatings under various annealing treatments were investigated using XRD and Rietveld refinement. The XRD pattern in **Fig. 5** illustrates structural changes in the PPNO coating as annealing temperature rises. Pr_6O_{11} was present in the as-deposited coating, with NiO and PrO_x emerging as the annealing temperature reaches 950 °C. Pr_2NiO_4 phase traces appear after annealing at 950 °C (4.94 wt.%) (**Fig.5b** and **Tab.3**). A

composite material with Pr_2NiO_4 (67.49 wt.%) and Pr_6O_{11} (32.51 wt.%) phases forms after annealing at 1000 °C.

In **Fig. 5a**, the peak positions of Pr_2NiO_4 and Pr_6O_{11} were shifted to higher angles compared to the ICSD database (PDF#01-086-0870 and 00-042-1121), likely due to internal stress from the coating, a known effect of magnetron sputtering deposition [18, 19]. The lattice contraction observed in Pr_2NiO_4 and Pr_6O_{11} after annealing at 1000 °C supports this. Specifically, Pr_2NiO_4 shows contraction in the a (5.4543 Å) and c (12.4429 Å) axes compared to PDF#01-086-0870 (a= 5.4567 Å, b= 5.3929 Å, c= 12.4464 Å), while Pr_6O_{11}'s lattice parameter decreases to 5.4614 Å from 5.4678 Å (PDF#00-042-1121) (**Fig.5b** and **Tab.3**). Increased annealing temperature correlates with lattice contraction, possibly due to phase transformation during crystallization. Additionally, higher temperatures promote grain growth, resulting in larger crystallite sizes for Pr_2NiO_4 compared to Pr_6O_{11} (**Tab.3**), which explains the larger particle size of Pr_2NiO_4 observed in morphology analysis (**Figs.6-8**).

Tab. 2 The deposition parameters for depositing PPNO cathode

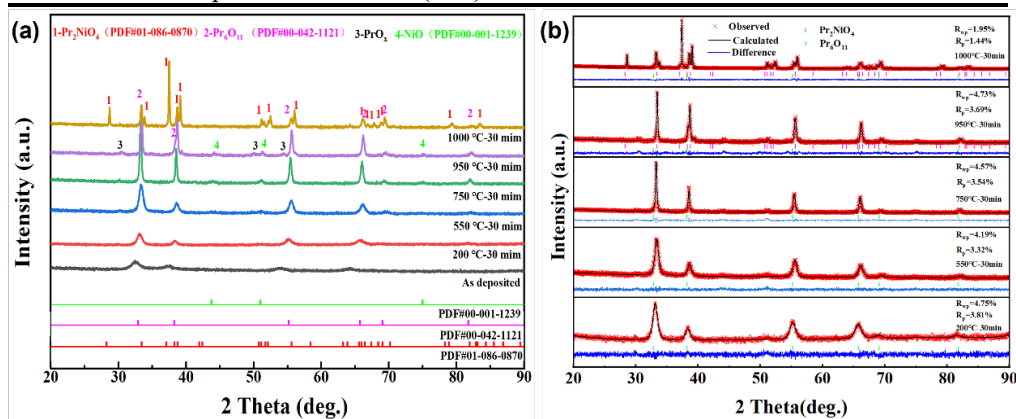| Deposition parameters		PPNO
Ar flow rate (sccm)		200
O_2 flow rate (sccm)		4.8-5.3
Total pressure (Pa)		1.9-2.1
Drawing distance(mm)		70
Frequency (kHz)		50
Toff (μs)		4
Pr target	Setpoint (%)	70
	Current (A)	2.5
Ni target	Power (W)	126
	Deposition thickness (mm)	5.9

Fig.5 XRD patterns of the PPNO cathode coating deposited on alumina pellet after various annealing treatments in air

Tab. 3 The lattice parameters and crystallite size of the PPNO coatings as function of the annealing temperature

Annealing temperature (°C)	Lattice parameters (Å)						Crystallite size (nm)		Percentage (wt.%)	
	Pr_2NiO_4			Pr_6O_{11}			Pr_2NiO_4	Pr_6O_{11}	Pr_2NiO_4	Pr_6O_{11}
	a	b	c	a	b	c				
As deposited	–	–	–	–	–	–	–	7.8	–	–
200	–	–	–	5.5006	5.5006	5.5006	–	10.3	–	–
550	–	–	–	5.4687	5.4687	5.4687	–	12.7	–	–
750	–	–	–	5.4657	5.4657	5.4657	–	32.6	–	–
950	5.3798	5.5189	12.4453	5.4635	5.4635	5.4635	62.3	40.6	4.94	95.06
1000	5.4543	5.4004	12.4429	5.4614	5.4614	5.4614	87.9	44.9	67.49	32.51

The porous morphology of the cathode coating is essential for facilitating oxygen diffusion. **Fig. 6** illustrates the morphological changes in the PPNO coating during the annealing treatment process. Initially, the PPNO coating appears dense (**Figs.6 a and d**) prior to annealing. However, evident macro-pores were observed after annealing at 950°C for 30 min (**Figs. 6 i** and **j**). The progression of annealing stages demonstrates the development of the porous structure in the PPNO cathode coating. Throughout the annealing process, the coating transitions from an amorphous to a crystalline state, with atomic migration within the coating due to the gain of energy [19-21]. During annealing at temperatures up to 750°C, micro (nano) pores were generated as a result of atomic migration (Pr and Ni), along with the crystallization of the coating. Subsequently, the micro (nano) pores aggregated into macro pores post-annealing at 950 °C (**Figs.6 i** and **j**). These sequential stages were marked by a volumetric expansion of the coating, likely attributed to the development of micro (nano) pores (**Tab.4**). Ultimately, the macro pores fused into larger pores following annealing at 1000 °C. Concurrently, small particles of Pr_6O_{11}-enriched form typical large particles of Pr_2NiO_4-enriched (**Figs. 6 k** and **l**). This stage was characterized by a volume reduction, induced by high-temperature sintering (**Tab.4**). Correspondingly, the porosity of the coating decreased from 44.8 ± 0.3 Vol. % at 950 °C to 42.9 ± 0.2 Vol.% at 1000 °C.

XRD and EDS analyses confirmed the presence of Pr_6O_{11} and Pr_2NiO_4-enriched regions in the PPNO cathode coating. Initially, Pr and Ni atoms in the deposited PPNO were uniformly distributed (**Figs.7c** and **8a**). However, after annealing treatment, atomic migration led to distinct phase transformations, with Pr and Ni concentrating in separate regions (**Figs. 7-8**). EDS data showed a higher Pr/Ni atomic ratio in smaller particles than in larger ones (**Figs. 7b** and **8c**), suggesting Ni enrichment in larger

particles and Pr in smaller ones. These observations align with XRD results, indicating that Ni-rich regions correspond to Pr_2NiO_4, while Pr-rich regions correspond to Pr_6O_{11}.

Tab. 4 The porosity and thickness of the PPNO coatings as function of the annealing temperature

Samples	Temperature (°C)	Cross-section porosity	Thickness (μm)
PPNO	As deposited		5.9 ± 0.2
	200	−	6.0 ± 0.1
	550	−	6.5 ± 0.2
	750	−	6.6 ± 0.2
	950	44.8 ± 0.3	7.5 ± 0.2
	1000	42.9 ± 0.2	6.9 ± 0.1
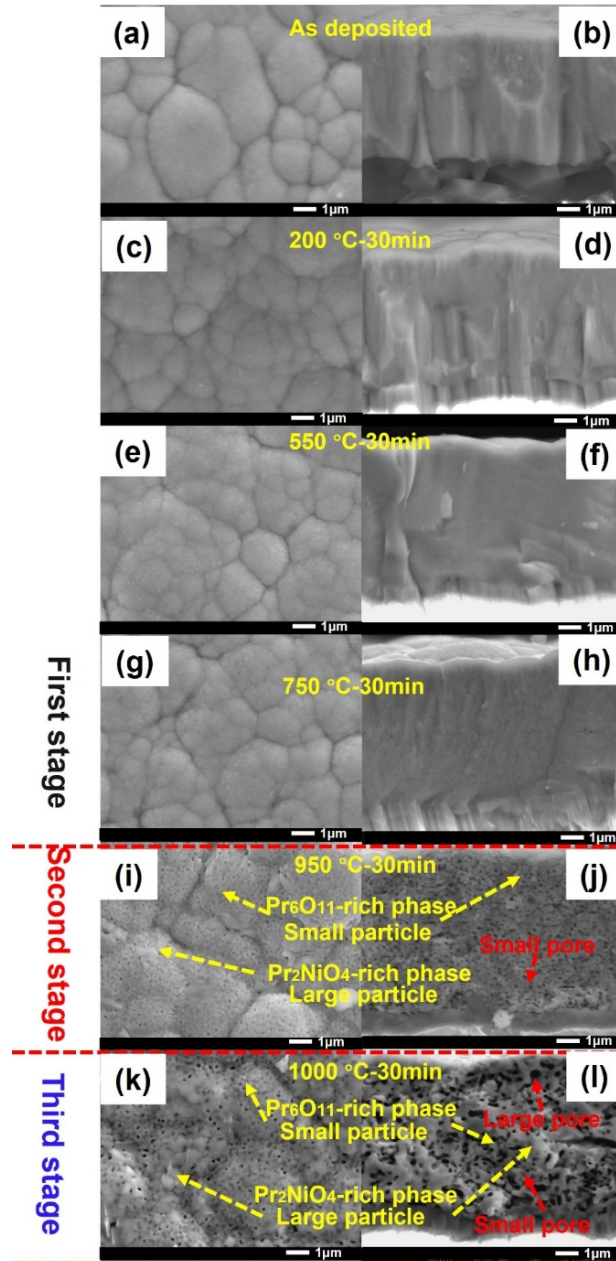
Fig.6 SEM images of the PPNO coatings after various annealing treatments: (a), (c), (e), (g), (i), and (k) refer to the surface; (b), (d), (f), (h), (j), and (l) refer to the cross-section
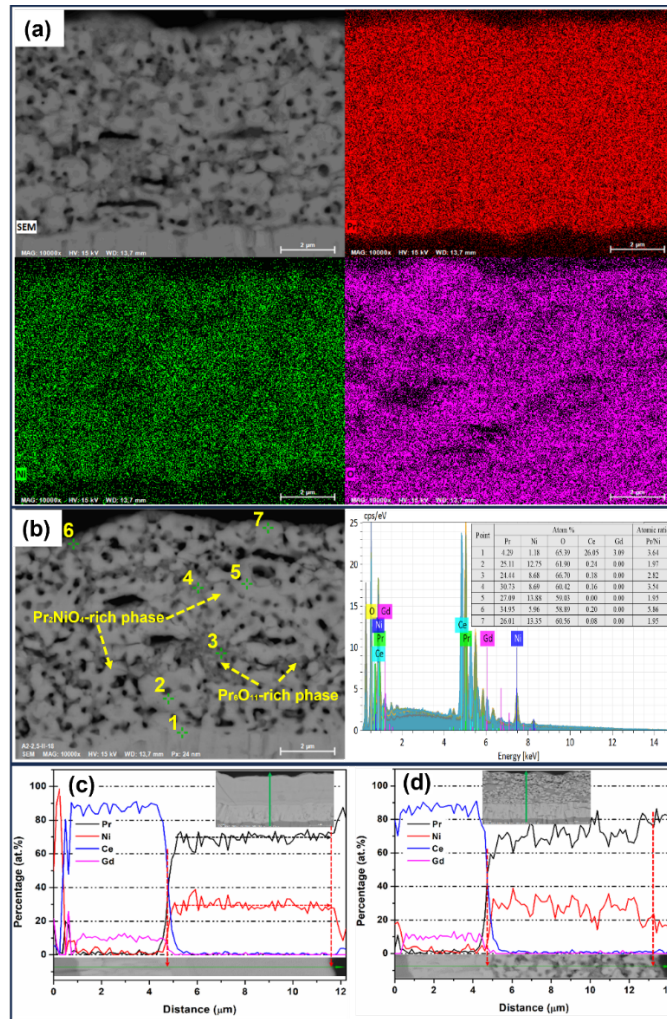
Fig.7 The cross-section SEM-EDS results of the polished PPNO cathode coatings: (a), (b) and (d) annealing at 1000°C for 30 min; (c) as deposited
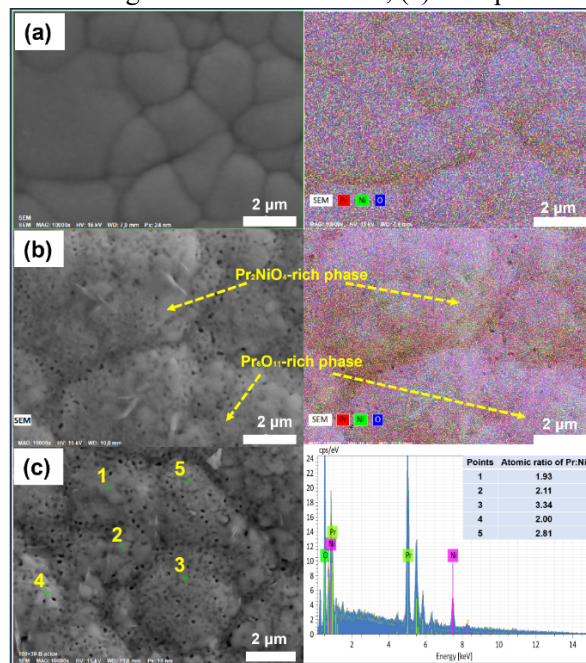

Fig.8 The surface SEM-EDS results of the PPNO cathode coatings: (a) as deposited, (b) and (c) annealing at 1000°C for 30 min

3.3 The characterization of electrochemical performance of PPNO cathode

The EIS results from symmetric cells (PPNO/8YSZ/PPNO) assessed the PPNO cathode's performance. ZView 2 software was employed to fit the impedance spectrum with an appropriate equivalent circuit model. As depicted in **Fig. 9a**, Nyquist plots of the symmetric cell (PPNO/8YSZ/PPNO) were recorded at temperatures from 600 to 750 °C in 50 °C increments. $LR_1(CPE_1//R_2)(CPE_2//R_3)(CPE_3//R_4)$ equivalent circuit model was selected to fit the impedance data. From the fitted model, resistances corresponding to various electrochemical processes were extracted to determine the cathode's R_p, a crucial indicator of its electrochemical performance. The mean capacitance and frequency relaxation for each semicircle contribution were calculated using the fitted data and applying Eqs. (1) and (2).

$$C = R^{((1-n)/n)} \times CPE^{1/n} \tag{1}$$

$$f_n = \frac{1}{2\pi(C_{eq_n}R_n)^{\frac{1}{n}}} \tag{2}$$

where R represents the electrical resistance, n is the decentering angle of the Constant Phase Element (*CPE*) function, and C denotes the capacitance associated with the phenomenon.

The capacitance effect (*C*) and frequency relaxation (*f*) were plotted against inverse temperature using a Schouler-type representation [22], serving as a reference for interpreting impedance diagrams. The Arrhenius plots (**Figs. 9b** and **c**) reveal that the lower capacitance (10^{-12} F) and higher frequency ($>10^5$ Hz) of R_2 at 600 and 650 °C for the symmetric cell are linked to the electrolyte response [23]. Consequently, R_2 was excluded from R_p and combined with R_1 as the electrolyte resistance, thus $R_p = R_3 + R_4$ (**Fig. 9a**). The first semicircle indicates an increase in capacitance (10^{-6} F) from 700 °C to 750 °C, corresponding to the electrode response [24]. Here, R_1 relates to the electrolyte response, and $R_p = R_2 + R_3 + R_4$. The R_p of PPNO cathode was presented in **Tab. 4,** with a low R_p at 750°C (0.08 $\Omega \cdot cm^2$), demonstrating strong competitiveness in the IT-SOFC cathode domain (**Tab.5**). This performance is attributed to the important contribution of Pr_6O_{11} in enhancing cathode ORR activity [25, 26].
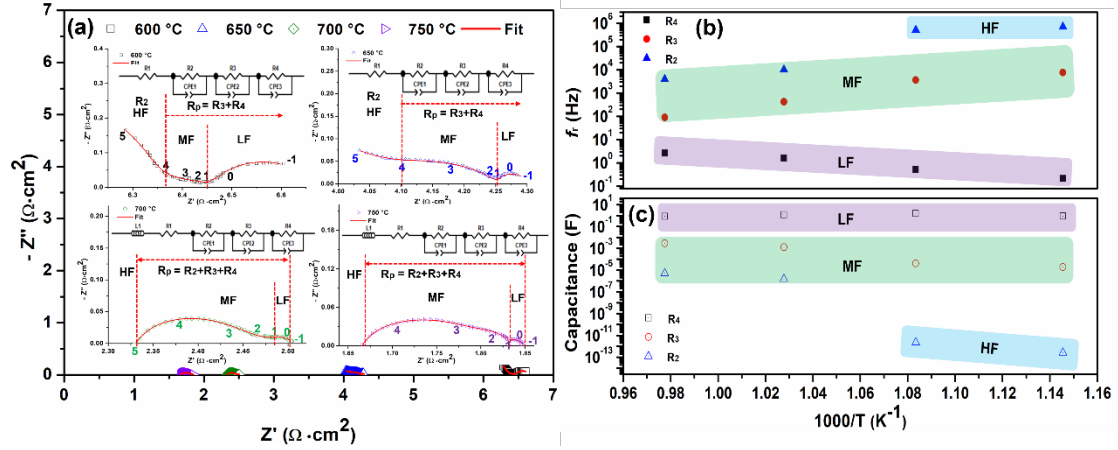
Fig.9 (a) Nyquist plots of PPNO electrode from 600 °C to 750 °C in air; Arrhenius plots of the relaxation frequencies (b) and the capacitances (c)

To elucidate the ORR process on the PPNO cathode and pinpoint the rate-controlling step, the polarization resistance (R_i) of PPNO across various frequency ranges and oxygen partial pressures (P_{O_2}) was measured by EIS test (**Fig.10**). **Fig. 10a** shows that R_p decreases as oxygen partial pressure increases, indicating enhanced ORR kinetics at the cathode. Concurrently, the ohmic resistance diminishes with the elevation of oxygen partial pressure. This phenomenon may be attributed to the heightened electronic conductivity of PPNO under increased oxygen partial pressure, consequently leading to a reduction in ohmic resistance [27, 28]. The relationship between R_i and P_{O_2} was described by Eq. (3) [29].

$$R_i \propto R_0 \left(P_{O_2} \right)^{-n} \tag{3}$$

Where R_i represents the values of R_p, R_{HF}, R_{MF}, and R_{LF} under different oxygen partial pressures. R_0 is a constant. The *n* values correspond to the reaction order of the ORR process.

The reaction order (*n* value) derived from fitting the experimental data using Eq. (3) was compared that from kinetic calculations to elucidate the PPNO cathode ORR process (**Tab.6**) [30]. As depicted in **Fig. 10b**, the *n* value for R_{HF} was 0.20, approximating 0.25, which indicates that the HF process corresponds to oxygen species reduction [31]. The *n* values for R_{MF} and R_{LF} were 0.53 and 0.82, respectively, nearing 0.5 and 1. This implies that both the MF and LF processes involve surface oxygen molecular dissociation, followed by diffusion of dissociated oxygen atoms to the TPB. The *n* value for R_p was closest to that of R_{MF}, suggesting that the MF region's impedance most significantly affects overall cathode polarization resistance. Consequently, the dissociation of molecular oxygen to atomic oxygen is inferred as the

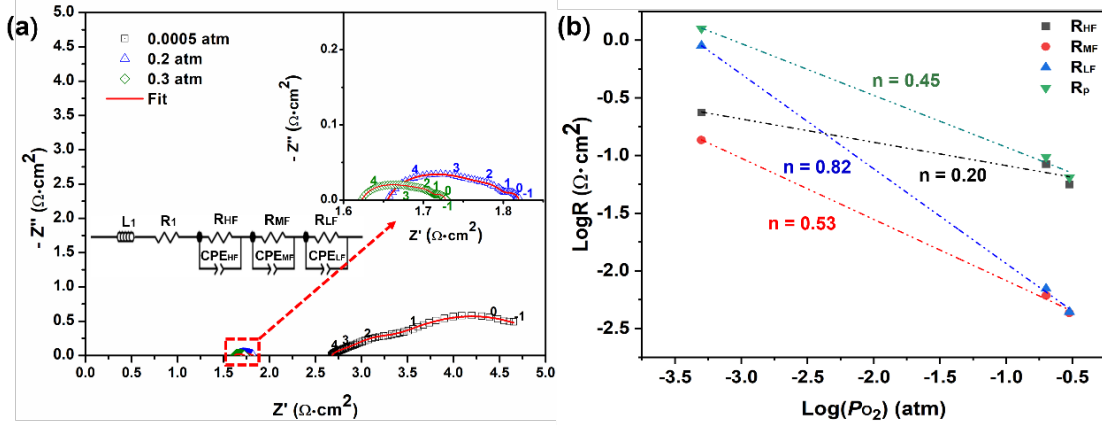rate-determining step in the cathode reaction, aligning with findings for Pr_6O_{11}-based cathodes [25, 32].

Fig.10 (a) Nyquist plot of PPNO electrode under different oxygen partial at 700 ℃; (b) dependence of resistances on oxygen partial pressure of PPNO electrode at 750 ℃

Tab. 5 Electrochemical properties of Pr_2NiO_4 and Pr_6O_{11} cathode for SOFCs: R_p values were obtained by symmetrical cell PPNO|GDC|PPNO testing.

Anode	Electrolyte	Cathode	$R_p(\Omega \cdot cm^2)$	Power density (mW/cm²)	OCV (V)	Refs.
Ni-YSZ	YSZ/GDC	PPNO	$0.08^{750\,℃}$	$1155^{750\,℃}$	$0.95^{750\,℃}$	This work
			$0.17^{700\,℃}$	$779^{700\,℃}$	$0.97^{700\,℃}$	
			$0.35^{650\,℃}$	$583^{650\,℃}$	$0.98^{650\,℃}$	
			$0.49^{600\,℃}$	$369^{600\,℃}$	$1.00^{600\,℃}$	
Ni-GDC	GDC	PNO	$0.18^{700\,℃}$	$327^{700\,℃}$	$0.68^{700\,℃}$	[30]
-	YSZ	PNO	$0.80^{750\,℃}$	-	-	[33]
Ni-YSZ	YSZ	LSM-Pr_6O_{11}	$0.08^{700\,℃}$	$1220^{800\,℃}$	$1.11^{750\,℃}$	[31]
Ni-YSZ	YSZ	Pr_6O_{11}	$0.03^{600\,℃}$	$500^{700\,℃}$	$1.08^{700\,℃}$	[34]
Ni-YSZ	YSZ/GDC	PPCO	$0.07^{700\,℃}$	$970^{700\,℃}$	1.12	[25]
Ni-YSZ	GDC	LSCF-Pr_6O_{11}	-	$118^{800\,℃}$	$1.06^{800\,℃}$	[26]
-	GDC	LSM- Pr_6O_{11}	$0.10^{650\,℃}$	-	-	[35]
SFM- Pr_6O_{11}	YSZ	SFM- Pr_6O_{11}	$0.10^{800\,℃}$	$455^{800\,℃}$	$1.04^{800\,℃}$	[36]
-	GDC	PSNO- Pr_6O_{11}	$0.114^{750\,℃}$	-	-	[37]

PNO: Pr_2NiO_4; LPNO: $La_{1.6}Pr_{0.4}NiO_4$; PPCO: $Pr_2CuO_4@Pr_6O_{11}$; LSM: $La_{0.8}Sr_{0.2}MnO_{3-\delta}$; LSCF: $La_{0.6}Sr_{0.4}Co_{0.2}Fe_{0.8}O_{3-\delta}$; SFM: $Sr_2Fe_{1.5}Mo_{0.5}O_{6-\delta}$; PSNO: $Pr_{1.2}Sr_{0.8}NiO_{4+\delta}$

Tab. 6 The relationship between *n* value and ORR step [31]

Steps	Elemental reactions	Reaction order
1	$O_{2,gas} \rightarrow O_{2,ads}$	n=1
2	$O_{2,ads} \rightarrow 2O_{ads}$	n=0.5
3	$O_{ads} + e' \rightarrow O'_{ads}$	n=0.375
4	$O_{ads} + e' + V \rightarrow O_o^x$	n=0.25
5	$O'_{ads} + e' \rightarrow O''_{ads}$	n=0.125
6	$O^x_{o,electrode} \rightarrow O^x_{O,electrolyte}$	0

To further assess the feasibility of the PPNO cathode, the I-V-P characteristics of NiO-YSZ|YSZ|GDC|PPNO single cell was determined (**Fig.11 and Tab.5**). This cell achieved a notable peak power density of 1155 mW·cm^{-2} at 750 °C (**Fig. 11b**). However, its OCV ranged from only 1.00 to .95 V between 600 and 750 °C (**Tab.5**), lower than literature values, primarily due to cracks in the YSZ|GDC electrolyte layer (**Fig.11a**). he single cell's long-term performance was evaluated by monitoring voltage at 700 °C under a constant current load of 0.4 A·cm^{-2}. The voltage degradation rate was merely 6.9 %, decreasing from 0.87 V to 0.81 V after 65 h, demonstrating the cell's excellent durability (**Fig. 11c**).
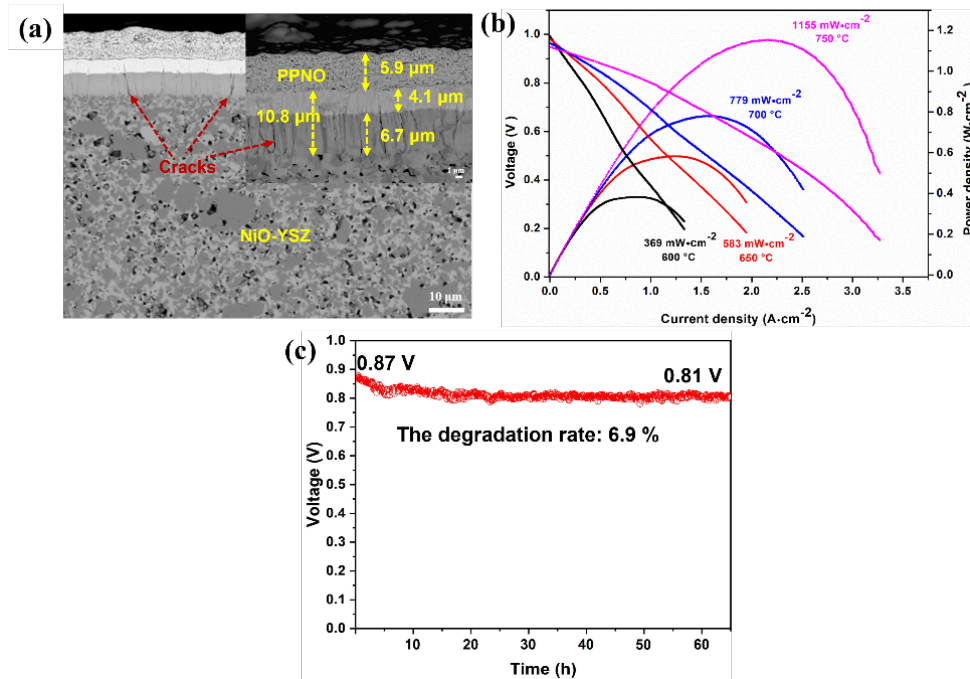

Fig.11 (a) NiO-YSZ|YSZ|GDC|PPNO single cell cross-section; (b) and (c) *I-V-P* characteristics and long-term stability test of the single cell, respectively

4. Conclusion

This work showcases the effective creation of porous, thin PPNO cathodes using the RMS technique. The remarkably low cathode R_p and superior single cell performance underscore the high electrocatalytic activity of the PPNO cathode, attributed to Pr_6O_{11}'s enhancement of the ORR process. The NiO-YSZ|YSZ|GDC|PPNO single cell delivers an output power of 1155 mW·cm^2 at 750 °C, highlighting its competitiveness in IT-SOFC applications. These results emphasize the potential of PPNO composites as SOFC cathodes and validate the use of RMS technology for developing porous, thin cathode layers for IT-SOFCs, potentially inspiring new cathode layer design strategies.

Authorship contribution statement

Xiaolei YE: methodology, formal analysis, investigation, data curation and writing - original draft. Hang LUO: formal analysis and writing - review & editing. Lei GAO: formal analysis. Shenghui GUO: funding acquisition, supervision. Li YANG: conceptualization, funding acquisition, writing - review & editing. Ming HOU: formal analysis. Kaihua CHEN: investigation, formal analysis. Yunchuan LI: formal analysis and software. Zhiguang HUA: formal analysis and software. Pascal BRIOIS：language review, formal analysis and visualization.

Conflict of Interest

The authors declare no conflict of interest.

Data availability

All data generated on analyzed during this study are included in this published article.

References

[1] Ndubuisi, A., Abouali, S., Singh, K., Thangadurai, V. Recent advances, practical challenges, and perspectives of intermediate temperature solid oxide fuel cell cathodes [J]. J Mater Chem A 2022; 10: 2196-227.

[2] Yuan, M.K., Gao, Y., Liu, L.M., Gao, J.T., Wang, Z., Li, Y., et al. High entropy double perovskite cathodes with enhanced activity and operational stability for solid oxide fuel cells [J]. J Eur Ceram Soc 2024; 44:3267-76.

[3] Wang, W., Su, C., Wu, Y., Ran, R., & Shao, Z. A comprehensive evaluation of a Ni–Al_2O_3 catalyst as a functional layer of solid-oxide fuel cell anode [J]. J Power Sources 2010; 195 (2): 402-411.

[4] Wachsman, E.D., Lee, K.T. Lowering the temperature of solid oxide fuel cells. Science [J]. 2011; 334: 935-9.

[5] Salman, M., Saleem, S., Ling, Y.H., Khan, M., Gao, Y. Improved electrochemical performance of high-entropy $La_{0.8}Sr_{0.2}FeO_3$-based IT-SOFC cathode [J]. Ceram Int 2025; 51: 4092-3.

[6] Yu, Y., Li, M., Chen George, Z. An overview of mixed ion-electron conducting (MIEC) perovskite oxides for solid oxide fuel cell (SOFC) cathode materials and relevant research in 2022 [J]. Sci Tech Rev 2023; 41: 74-88.

[7] Jiang, S.P. Development of lanthanum strontium cobalt ferrite perovskite electrodes of solid oxide fuel cells - A review [J]. Int J Hydrogen Energ 2019; 44: 7448-93.

[8] Liao, Z.H., Yang, Y.P., Ou, D.R., Tang, Y., Wang, B., He, B.B., et al. Enhanced oxygen electrode performance in solid oxide fuel cells La-doping of $Pr_2NiO_{4+\delta}$-based Ruddlesden-Popper perovskites [J]. J Mater Chem C 2024; 12: 19506-14.

[9] Ren, Q.H., Zhang, Y., Tao, H.L., Qin, L., Swierczek, K., Guan, W.B., et al. An innovative and facile synthesis route of $(La,Sr)_2FeO_{4+\delta}$-$La_{0.4}Sr_{0.6}FeO_{3-\delta}$ composite as a highly stable airelectrode for reversible solid oxide cell applications [J]. J Adv Ceram 2024; 13: 1337-48.

[10] Noh, H.-S., Yoon, K.J., Kim, B.-K., Je, H.-J., Lee, H.-W., Lee, J.-H., et al. The potential and challenges of thin-film electrolyte and nanostructured electrode for yttria-stabilized zirconia-base anode-supported solid oxide fuel cells [J]. J Power Sources 2014; 247: 105-11.

[11] Yang, Y., Zhang, Y., Yan, M. A review on the preparation of thin-film YSZ electrolyte of SOFCs by magnetron sputtering technology [J]. Sep Purif Technol 2022; 298: 121627.

[12] Liang, F., Pan, Z., Wang, H., Jiao, Z., Yan, Z., Shen, X., ... & Wu, J. Scalable and

facile fabrication of tri-layer electrolytes by reactive sputtering for efficient and durable solid oxide fuel cells [J]. Chem Eng J 2024; 484: 149523.

[13] Solovyev, A., Sochugov, N., Rabotkin, S., Shipilova, A., Ionov, I., Kovalchuk, A., et al. Application of PVD methods to solid oxide fuel cells [J]. Appl Surf Sci 2014; 310: 272-7.

[14] Fondard, J., Billard, A., Bertrand, G., Fourcade, S., Batocchi, P., Mauvy, F., et al. Effect of total pressure on La_2NiO_4 coatings deposited by reactive magnetron sputtering using plasma emission monitoring [J]. Surf Coat Tech 2016; 295: 29-36.

[15] Fondard, J., Billard, A., Bertrand, G., Briois, P. Synthesis and characterization of $La_2NiO_{4+\delta}$ coatings deposited by reactive magnetron sputtering using plasma emission monitoring [J]. Solid State Ionics 2014; 265: 73-9.

[16] Billard, A., Frantz, C. Attempted modelling of thickness and chemical heterogeneity in coatings prepared by dc reactive magnetron sputtering [J]. Surf Coat Tech 1993; 59: 41-7.

[17] Ye X. Development of Metal-Supported Solid Oxide Fuel Cell (MS-SOFC) by Atmospheric Plasma Spraying and Reactive Magnetron Sputtering Technique [D]. Université Bourgogne Franche-Comté, 2023.

[18] Luo, H., Sun, H., Ye, X., et al. Incorporation of SiC on the mechanical properties, tribological performance, and oxidation resistance of HfC-SiC/aC: H coatings prepared by hybrid HiPIMS and pulsed-DC magnetron co-sputtering[J]. Ceram Int 2023; 49 (24): 40486-40497.

[19] Kelly, P.J., O'Brien, J., Arnell, R.D. The production of porous and chemically reactive coatings by magnetron sputtering [J]. Vacuum 2004; 74 (1): 1-10.

[20] Masłyk, M., Borysiewicz, M.A., Wzorek, M., et al. Influence of absolute argon and oxygen flow values at a constant ratio on the growth of Zn/ZnO nanostructures obtained by DC reactive magnetron sputtering [J]. Appl Surf Sci 2016; 389: 287-293.

[21] Jaiswal, J., Chandra, R., Tsuchiya, K. Sputtered Grown Porous Nanostructured Materials: Achievements and Advances in Gas Sensing[M]//Materials for Electronic, Magnetic, and Spintronic Technologies: Characterization and Applications from Energy Storage to Disease Detection. Cham: Springer Nature Switzerland 2024: 109-132.

[22] Schouler, E., Kleitz, M. Electrocatalysis and inductive effects at the gas, Pt/stabilized zirconia interface [J]. J Electrochem Soc 1987; 134: 1045.

[23] Adler, S.B. Mechanism and kinetics of oxygen reduction on porous La_{1-}

$_x$Sr$_x$CoO$_{3-\delta}$ electrodes [J]. Solid State Ionics 1998; 111: 125-34.

[24] Dailly, J., Fourcade, S., Largeteau, A., Mauvy, F., Grenier, J.-C., Marrony, M. Perovskite and A$_2$MO$_4$-type oxides as new cathode materials for protonic solid oxide fuel cells [J]. Electrochim Acta 2010; 55: 5847-53.

[25] Shijie, Z., Na, L., Liping, S., Qiang, L., Lihua, H., Hui, Z. One-pot synthesis Pr$_6$O$_{11}$ decorated Pr$_2$CuO$_4$ composite cathode for solid oxide fuel cells [J]. Int J Hydrogen Energ 2022; 47: 6227-36.

[26] Kim, Y., Luo, J., Park, S., An, S., Yeom, E., Li, O.L. Robust Pr$_6$O$_{11}$ infiltration for La$_{0.6}$Sr$_{0.4}$Co$_{0.2}$Fe$_{0.8}$O$_{3-\delta}$ cathode performance enhancement on electrolyte supported solid oxide fuel cells [J]. Curr Appl Phys 2024; 59: 39-45.

[27] Song, J., Ning, D., Boukamp, B., et al. Structure, electrical conductivity and oxygen transport properties of Ruddlesden–Popper phases Ln$_{n+1}$Ni$_n$O$_{3n+1}$ (Ln= La, Pr and Nd; n= 1, 2 and 3) [J]. J Mater Chem A 2020; 8(42): 22206-22221.

[28] Ishihara, T. Oxide ion conductivity in defect perovskite, Pr$_2$NiO$_4$ and its application for solid oxide fuel cells [J]. J Ceram Soci Japan 2014; 122 (1423): 179-186.

[29] Zhong, F., Li, Z., Luo, Y., Chen, C., Zhou, C., Lin, L., et al. Geometric structure distribution and oxidation state demand of cations in spinel Ni$_x$Fe$_{1-x}$Co$_2$O$_4$ composite cathodes for solid oxide fuel cells [J]. Chem Eng J 2021; 425: 131822.

[30] Han, Z., Bai, J., Chen, X., Zhu, X., Zhou, D. Novel cobalt-free Pr$_2$Ni$_{1-x}$Nb$_x$O$_4$ (x= 0, 0.05, 0.10, and 0.15) perovskite as the cathode material for IT-SOFC [J]. Int J Hydrogen Energ 2021; 46: 11894-907.

[31] Zamudio-García, J., Caizán-Juanarena, L., Porras-Vázquez, J. M., et al. Unraveling the influence of the electrolyte on the polarization resistance of nanostructured La$_{0.6}$Sr$_{0.4}$Co$_{0.2}$Fe$_{0.8}$O$_{3-\delta}$ cathodes [J]. Nanomaterials 2022; 12 (22): 3936.

[32] Zamudio-García, J., Caizán-Juanarena, L., dos Santos-Gómez, L., et al. Enhanced thermal and electrochemical properties in La$_{0.8}$Sr$_{0.2}$MnO$_{3-\delta}$-Pr$_6$O$_{11}$ nanocomposite cathodes for solid oxide fuel cells [J]. Int J Hydrogen Energ 2025; 126: 552-561.

[33] Fondard, J., Billard, A., Bertrand, G., Briois, P. Ln$_2$NiO$_{4+\delta}$ (Ln= La, Pr, Nd) coatings deposited by reactive magnetron sputtering as cathode material for intermediate temperature solid oxide fuel cell. Vacuum 2018; 152: 97-108.

[34] Sharma, R.K., Djurado, E. An efficient hierarchical nanostructured Pr$_6$O$_{11}$ electrode for solid oxide fuel cells[J]. J Mater Chem A 2018; 6 (23): 10787-10802.

[35] Caizán-Juanarena, L., Zamudio-García, J., Marrero-López, D. Electrochemical

investigation of Pr_6O_{11} infiltration into $La_{0.8}Sr_{0.2}MnO_{3-\delta}$-$Ce_{0.9}Gd_{0.1}O_{1.95}$ cathodes for IT-SOFC [J]. Ceram Int 2023; 49 (21): 33717-33724.

[36] Zhu, Z., Sun, K., Xu, D., et al. Enhancing the performance of symmetrical solid oxide fuel cells with $Sr_2Fe_{1.5}Mo_{0.5}O_{6-\delta}$ electrodes via infiltration of Pr_6O_{11} bifunctional catalyst [J]. Electrochim Acta 2022; 402: 139569.

[37] Liu, Y., Kang, K., Pan, Z., et al. Enhancing the oxygen reduction reaction activity of SOFC cathode via construct a cubic fluorite/perovskite heterostructure [J]. Appl Surf Sci 2024; 642: 158405.